CFD-DEM Investigation on van der Waals Force in Gas-Solid Bubbling Fluidized Beds

S.M. Okhovat-Alavian[1], H.R. Norouzi[2] and N. Mostoufi*[1]

1. Process Design and Simulation Research Center, School of Chemical Engineering, College of Engineering, University of Tehran, P.O. Box 11155-4563, Tehran, Iran.
2. Depatment of Chemical Engineering, Amirkabir University of Technology (Tehran Polytechnic), PO Box: 15875-4413, Hafez 424, Tehran, Iran.

Abstract

Effect of interparticle force on the hydrodynamic of gas-solid fluidized beds was investigated using the combined method of computational fluid dynamics and discrete element method (CFD-DEM). The cohesive force between particles was considered to follow the van der Waals form. The model was validated by experimental results in terms of bed voidage distribution and Eulerian solid velocity field. The results revealed that the incorporated model can satisfactorily predict the hydrodynamics of the fluidized bed in the presence of interparticle forces. Effect of interparticle force on bubble rise characteristics such bubble stability, bubbles diameter and bubble velocity, was investigated. It was shown that emulsion voidage increases with the interparticle force in the bed and it can hold more gas inside its structures. In addition by increasing interparticle force, the bubble size and bubble rise velocity increase while the average velocity of particles decreases.

1. Introduction

Gas–solid fluidized beds are used in a variety of industrial processes due to uniform bed temperature, high mass and heat transfer rates and suitability for large-scale operations [1]. Based on their fluidization behavior, powders are categorized into four groups according to their size and density, called Geldart A, B, C and D [10]. However, experimental evidences indicate that particle size and density cannot be taken as the only characteristic parameters for predicting the fluidization behavior of particles [21, 38]. Many experiments have been done to investigate the influence of Interparticle forces (IPFs) on the fluidization behavior of gas-solid fluidized beds. These experiments include reducing the mean particle size to increase the van der Waals force [3, 11, 12], adding a cohesive agent into the bed to increase the capillary force [5,12], using a magnetic field around the bed [1], increasing the bed temperature [18, 19] and coating of particles with a polymer [28, 29, 31]. Experimental results indicated that IPF is among the most important factors that increasing of which can alter the fluidization behavior from Geldart group B to group A

* Corresponding Author.
Tel.: (+98-21) 6696-7781
Fax: (+98-21) 6695-7784
Email: mostoufi@ut.ac.ir (N. Mostoufi)

and then group C. Increase in IPFs increases minimum fluidization velocity, transition velocity from bubbling to turbulent fluidization, the tendency of gas passing through the emulsion and bubble size [29].

Although the experimental measurements have provided proper understanding of hydrodynamic changes of gas-solid flows in the presence of IPFs. However, much is to be known about particle-scale phenomena and the mechanisms governing the hydrodynamics of fluidization (e.g., change in the minimum fluidization velocity, change in bubble diameter, etc.) in the presence of IPFs, which can hardly be obtained through experiment. Therefore, numerical simulations can be used to overcome the difficulties of experiments and to obtain detailed information about such phenomena. Among various approaches for modeling fluidized beds, the combination of discrete element method (DEM) [6] and computational fluid dynamics (CFD) [34] is among the promising ones. In this approach, particles form the discrete phase and each individual particle is tracked in time and space by integrating the Lagrangian equation of motion while gas is assumed to be the continuum phase and its flow characteristics are obtained by solving the volume averaged Navier-Stokes equation. Yu and Xu [41] and Ye et al. [40] used the CFD-DEM technique and included the van der Waals force to study the fluidization behavior of group A particles. They found that the regime is homogeneous when the van der Waals force is relatively weak. Rhodes et al. [25] added a cohesive force between particles in their simulations and demonstrated that the fluidization characteristics of Geldart group B or D particles change to Geldart Group A. The most important change in this case was observing non-bubbling fluidization for gas velocities between the minimum fluidization and the minimum bubbling which are the group A fluidization characteristics. Pandit et al. [23] studied the effect of van der Waals force on formation and characteristics of bubbles and found that in the presence of high level of van der Waals force, not only does the bubble formation process require a higher air velocity for its initiation, but also it is slower when compared to the case with no van der Waals force. Kaboyashi et al. [14-16] also showed that the bed pressure drop hysteresis during fluidization and defluidization processes can be observed and the spring stiffness constant used in

the DEM model has a significant influence on the adhesive behavior of particle to the wall.

Effect of IPFs on bubble dynamics (i.e., bubble diameter and rise velocity in a gas fluidized bed) has not been studies properly yet. To fill this gap in the fluidization process, a CFD–DEM study was conducted in this work to describe the characteristics of bubbles in a two-dimensional fluidized bed at different level of cohesive interparticle force. The results of probability density distribution of the instantaneous local bed voidage and volume-averaged solid velocity field were compared with experimental results available in literature to validate the model. The influences of IPFs on the bubble characteristics, stability, diameter and velocity were then investigated.

2. Numerical Model

In the CFD-DEM approach, particles are assumed to be the discrete phase and gas is assumed to be the continuum phase. For the contacts between particles, the soft-sphere approach was used in which particles can overlap partially, hence, particles can have multiple contacts [6]. The gas phase motion is described by the volume-averaged Navier-Stokes equation over an Eulerian mesh. The coupling between phases is done through inter-phase momentum transfer (i.e., drag and pressure gradient forces) and gas volume fraction. Since the density of solid particle is much greater than the density of gas, the buoyant force acting on each particle was ignored. The governing equations are described in the followings.

2.1. Governing equations for particles

Translational and rotational motions are considered for each particle. The translational motion of each spherical particle i, described by the Newton's second law of motion, and the rotational motion are given by [37]:

$$m_i \frac{d\vec{v}_i}{dt} = m_i \frac{d^2\vec{r}_i}{dt^2} = \sum_{j=1}^{n_c} \vec{f}^{\,c}_{ij} + \vec{f}_{d,i} + f_g + \vec{f}_{vdW} \quad (1)$$

$$I_i \frac{d\omega_i}{dt} = \sum_{j=1}^{k_t} \vec{M}^{\,t}_{ij} \quad (2)$$

The terms on the right-hand side of Eq. (1) are sum of contact forces, fluid-drag force, gravitational force and sum of cohesive forces, respectively. The contact forces between particle-particle and particle-wall (wall as particle j with infinity radius) are composed of normal $\vec{f}_{ij}^{\,n}$ and tangential $\vec{f}_{ij}^{\,t}$ components. The cohesive force consists of particle-particle and particle–wall cohesive forces. The expressions used to calculate the forces and torques are given in Table 1.

2.2. Cohesive force

In this study, the cohesive force between two particles and between particles and wall, was assumed to follow the van der Waals form. A particle may interact with its surrounding particles (n_k particles) via the van der Waals force. In this work, the Verlet list was employed to detect interparticle interactions and a cut-off radius was considered for the van der Waals force. Fig. 1 shows the schematic of the Verlet list of a target particle.
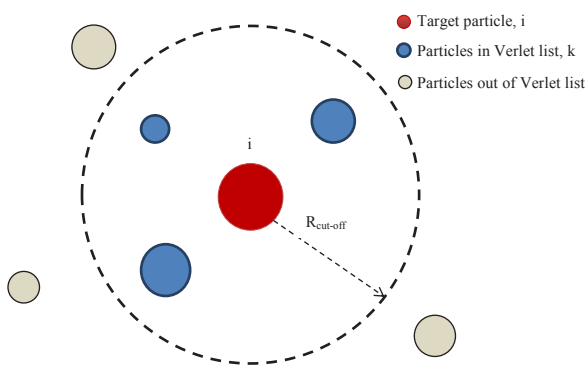
Figure 1. The Verlet list of a target particle i

According to this approach, all particles around the target particle that lie within a sphere with radius $R_{cut\text{-}off}$ are considered in the Verlet list of the target particle. Since particles move a very short distance in each integration time step, list remains unchanged in several time steps. This prevents redundant updates of the Verlet list during the simulation which is the main advantage of this method. In the present work, the cut-off radius, $R_{cut\text{-}off}$, for the target particle was assumed to be the distance beyond which the van der Waals

force becomes less than 5% of weight of the particle.

As shown in Table 1, the van der Waals force is a function of the surface distance between particles or between particle and wall. When the particles or particle and wall are in contact, an unrealistic large van der Waals force would be obtained from the equations of Table 1. To solve this problem, a minimum separation distance of 0.4 nm is considered between particles and particle and wall [16, 33].

2.3. Governing equations for fluid

The volume-averaged continuity and Navier–Stokes are [2]:

$$\frac{\partial\left(\varepsilon\rho_f\right)}{\partial t} + \nabla.\left(\varepsilon\rho_f\,\vec{u}\right) = 0 \tag{3}$$

$$\frac{\partial\left(\varepsilon\rho_f\,\vec{u}\right)}{\partial t} + \nabla.\left(\varepsilon\rho_f\,\vec{u}\vec{u}\right) = \\ -\varepsilon\nabla p_f - \overline{F}_{fp} - \varepsilon\nabla.\left(\tau\right) + \varepsilon\rho_f\,g \tag{4}$$

The term $\overline{F}_{fp}$ represents the average momentum exchange term between the solid and gas phases:

$$\overline{F}_{fp} = \sum_i^{k_c} \frac{\overline{f}_{d,i}}{V_C} \tag{5}$$

where V_c is volume of the fluid cell.

2.4. Coupling

Equations of gas and the solid phases are coupled through porosity and fluid–particle interaction force, $\overline{F}_{fp}$. Various schemes for coupling the interphase momentum interactions can be considered as reviewed by Feng et al. [9]. According to their recommendation, the forces acting on each particle should be computed through the fluid volume fraction and local fluid velocity in each fluid cell. The obtained forces are substituted in the equation of motion, Eq. (1), for each particle and then integrated over time to calculate new velocities and positions of particles. The particle–fluid interaction force in each fluid cell is then calculated by Eq. (5). More information and ex-

planation about the coupling process are provided by Norouzi et al. [22].

The solid volume fraction is calculated through the volume occupied by the particles in each fluid cell:

$$\varepsilon_{3D} = 1 - \frac{1}{V_C} \sum_{i=1}^{k_c} \alpha_{cell}^i V_{p,i} \qquad (6)$$

Where α_{cell}^i and $V_{p,i}$ are fractional volume of particle i presenting in each cell and volume of that particle, respectively. In the present work, the size of fluid cell was larger than the particle size (at least 4 times) but smaller than the macroscopic structures in the bed (i.e., bubbles). The SIMPLE (Semi-Implicit Method for Pressure-Linked Equations) algorithm [24] was applied to solve the gas phase equations.

The first order up-wind scheme was utilized for the convection terms. The Eulerian cell size was 2.3 mm (4 times greater than the particle diameter). In the case of the fluid velocity, the no-slip boundary condition was used to the walls and the fully developed condition to the exit at the top. An in-house code written in FORTRAN was used for the simulations [13].

Table 1. Relations for evaluating various forces acting on particle i.

Force	Type	Symbol	Formula
contact forces [17]	normal	$\vec{f}_{ij}^{\,n}$	$-(k_n \delta_n)\overline{n_{ij}} - (\eta_i \vec{V}_{r,ij} . \vec{n}_{ij})\vec{n}_{ij}$
	tangential	$\vec{f}_{ij}^{\,t}$	$-\left(\min\left(\mu \left| \vec{f}_{ij}^{\,n} \right|, \left| k_t \delta_t \vec{t}_{ij} \right| \right) \frac{\delta_t}{|\delta_t|} \right) \vec{t}_{ij} - \eta_i \vec{V}_{t,ij}$
torque	-	$\overline{M}_{ij}^{\,t}$	$\overline{R}_i \times \vec{f}_{ij}^{\,t}$
gravity	-	$\vec{f}_{g,i}$	$m_i g$
van der Waals forces [7]	particle-particle	$\vec{f}_{vdw,ik}$	$H \dfrac{d_p}{24 h_{ij}^2}$
	particle-wall	$\vec{f}_{vdw,i \to w}$	$H \dfrac{d_p}{12 h_{iw}^2}$
fluid drag force [8]		$\vec{f}_{d,i}$	$\hat{f}_{d,i} = 3\pi d_{p,i} \mu_f \varepsilon (\vec{u} - \vec{v}_i)$
			$\hat{f}_{d,i} = \dfrac{C_d}{24} \mathrm{Re}_p \, \varepsilon^{-\chi}$
			$\chi = 3.7 - 0.65 \exp(-0.5(1.5 - \log_{10} \mathrm{Re}_p))$
			$C_d = (0.63 + 4.8 \mathrm{Re}_p^{-1/2})^2$

$$\overline{R}_i = \vec{r}_j - \vec{r}_i, \, \vec{n}_{ij} = \frac{\overline{R}_i}{|\overline{R}_i|}, \overline{V}_{r,ij} = \overline{V}_i - \overline{V}_j, \hat{\omega}_{ij} = \frac{\overline{\omega}_i - \overline{\omega}_j}{|\overline{\omega}_i - \overline{\omega}_j|}, \mathrm{Re}_p = \frac{\rho_f d_{p,i} \varepsilon |\vec{u} - \vec{v}_i|}{\mu_f}$$

Table 2. Experimental and simulation conditions and parameters

Simulation					
Particles		Gas		Bed	
Shape	Spherical	Fluid	Air	Width (m)	0.0504
Number of particles	155000	CFD cell size (mm^2)	2.4 × 2.4	Height (m)	0.4
Particle diameter (m)	0.00058	Viscosity (kg/m.s)	1.85×10^{-5}	Thickness (m)	0.0058
Density (kg/m^3)	1556	Bed distributor	Porous plate		
Initial height (m)	0.085	Pressure (MPa)	0.1		
Spring constant (N/m)	1000	Density (kg/m^3)	1.2		
Sliding friction coefficient	0.3	U_{mf} (m/s)	0.16		
Restitution coefficient	0.9	Superficial velocity (m/s)	0.35, 0.6, 0.9		
Time step (s)	0.5×10^{-5}	Time step (s)	0.5×10^{-4}		
Experiment					
Particles		Gas		Bed	
Shape	Spherical	Fluid	Air	radius (m)	0.152
Diameter (μm)	580	Viscosity (kg/m.s)	1.85×10^{-5}	Height (m)	3
Density (kg/m^3)	1556	Bed distributor	Porous plate		
Initial height (m)	0.26	Pressure (MPa)	0.1		
		Density (kg/m^3)	1.2		
		Superficial velocity (m/s)	0.35, 0.6, 0.9		

3. Experimental Data and Simulation Conditions

3.1. Experimental data

In order to validate the model, the numerical results probability density distribution of the instantaneous local bed voidage and volume-averaged solid velocity field were compared with experimental results of Shabanian and Chaouki [28, 29] at various values of IPF. Shabanian and Chaouki [2011] applied a polymer coating approach to increase and adjust the level of IPFs in a gas–solid fluidized bed. Their method was based on coating spherical inert particles with a polymer with a low glass transition temperature. In the present work, the data obtained by Shabanian and Chaouki [28,29] were utilized for validation of the model. Uncoated (fresh) and coated sugar beads (d_p = 580 μm, ρ_p = 1556 kg/m^3) were separately used in the fluidized bed at various operating temperatures to investigate the effect of IPF on the hydrodynamics of a gas–solid fluidized bed. The initial bed height was 26 cm (H/D_c≈1.70), i.e., 4.0 kg of powder. The magnitude of IPF was controlled by temperature of the inlet air. The bed temperature was changed near and slightly above the glass transition temperature of the polymer, between 20 and 40 °C. For simplicity, the tests at various operating temperatures are called in shortened form of SB20, CSB30, CSB35

and CSB40, which stand for uncoated sugar beads at 20 °C and coated sugar beads at 30, 35, and 40 °C, respectively. Before the work of Shabanian and Chaouki [31], Buoffard et al. [4] also applied the same approach and material. They estimated the adhesion energy for the coated polymer by measuring the pull-off force. Their results illustrated that the magnitude of IPFs is in the same range of van der Waals force.

3.2. Simulation conditions

A rectangular bed filled with particles of the same in size and density in the experiments and air as the fluidizing gas, were considered in the simulations. It is worth mentioning that the number of particles in experiments was very large such that its simulation is not feasible with the existing computational resources. To overcome this problem and reduce the simulation time, number of particles was reduced by considering a smaller bed. The same aspect ratio L/D_c =1.7 was considered in both simulations and experiments, based on which the bed width in simulations was considered to be 5.04 cm. All the needed data (pressure and voidage) were recorded from the center of the bed in order to avoid the wall effect. The properties of bed, particles and air are listed in Table 2. All the simulations were continued for 15 s in real time.

Table 3. Calculated Hamaker constants at various bed temperatures

system	Temperature (°C)	Hamaker constant (J)	$\overline{f}_{vdW}\big/f_g$
SB20	20	0	0
CSB20	20	2.68×10^{-19}	26
CSB30	30	3.6×10^{-19}	35
CSB35	35	5.46×10^{-19}	53
CSB40	40	7.21×10^{-19}	70
CSB45	45	9.7×10^{-19}	94

Table 4. Comparison of the dominant frequency for 3D and 2D beds using Equation (10)

Hamaker constant (J)	Bubble diameter (m)	Ratio of frequencies	Bubble frequency in experiment (Hz)	Bubble frequency in 2D simulation (Hz)	Bubble frequency for 3D bubble (Hz)
0	0.049	0.206	1.24	7.62	1.49
3.6×10^{-19}	0.0504	0.207	1.36	7.8	1.6

Hamaker constants, which are proportional to the magnitude of the IPF, were calculated from the results reported by Buoffard et al. [4]. The calculated cohesive force was considered as the maximum magnitude of van der Waals force. This maximum occurs when the surface distance between particles or a particle and a wall, *h*, is the minimum separation distance of 0.4 nm. Hence, the Hamaker constant was calculated by considering the van der Waals force to be equal to the cohesive force reported by Buoffard et al. [4] and the minimum separation distance. The Hamaker constants as well as relative cohesive forces (with respect to the weight of a particle) are given in Table 3 at various bed temperatures. In this table, the maximum van der Waals force is cohesive force used throughout this work.

4. Result and Discussion

4.1. Validation

In this study, the simulation results were validated with experimental data of Shabanian and Chaouki [14, 15]. In their work, the instantaneous local bed voidage was measured by an optical fiber probe at various gas velocities in the bubbling regime of fluidization. The fiber probe was positioned at the bed center at an axial position 20 cm above the distributor plate. The probability density distribution of instantaneous local bed voidage and the Eulerian solid velocity field were compared with experimental data for validating the model.

4.1.1. Bed voidage distribution

The probability density distributions of the local bed voidage for SB20 and CSB30 at gas velocity of 0.9 m/s were taken from Shabanian et al. [14] .The simulated probability density distributions of the local bed voidage at Hamaker constants of 0 J (corresponding to SB20) and 3.6×10^{-19} J (corresponding to CSB30) at the superficial gas velocity of 0.9 m/s were also obtained and compared with the experimental results in Fig. 2. This figure shows that there are two peaks in the local voidage distribution of both beds. The first peak at low voidage represents the emulsion phase and the second peak at high voidage is related to the bubble phase. It can be seen in Fig. 2 that there is a good agreement between simulated and experimental values.

4.1.2. Eulerian solid velocity field

For determining the Eulerian solid velocity field, bed width and bed height were divided into 20 and 80 equal parts, respectively, which resulted in having cells with size of 0.0025×0.005 m. The particles were counted in each cell at each time step. Then, the summation of velocities of particles in the same cell was divided by the number of particles in that cell to obtain the averaged particle velocity. This averaging was done for the time span of 1 s.

The experimental Eulerian solid velocity fields for SB20 and CSB40 at superficial gas velocities of 0.3 and 0.5 m/s by Shabanian and Chaouki [28] are presented in Fig. 3.
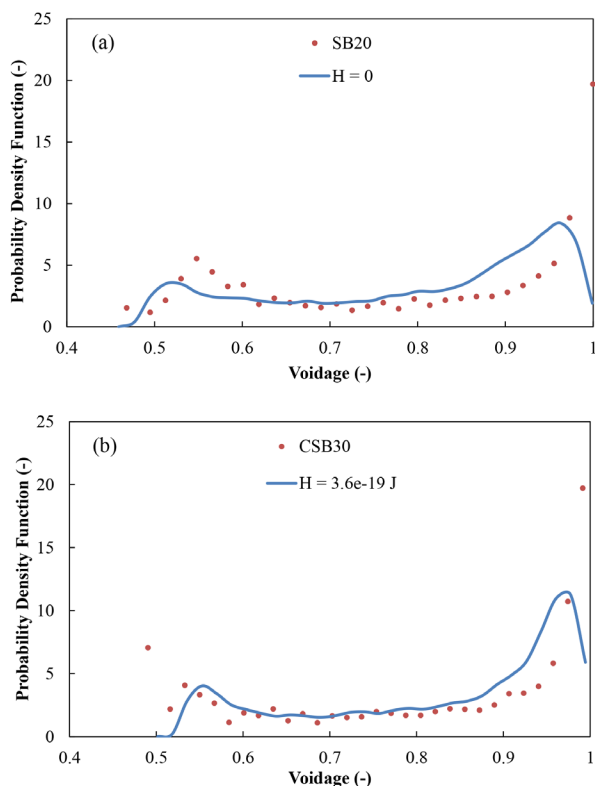
Figure 2. Comparison of simulated and experimental probability density distribution of local bed voidage at U_g = 0.9 m/s (a) non-cohesive particles, (b) cohesive particles [14]

This figure shows that there is a similar solid flow pattern in all cases, which is rising of particles to the splash zone through the central region of the bed and falling along the annulus. However, the solid flow pattern for CSB40 at 0.3 m/s diverged from the typical pattern, which is upward movement along the annulus in the bottom layer and identical to the typical solid flow pattern above the intermediate layer. In simulation, solid average velocity was calculated for beds with Hamaker constants of 0 J and $7.2×10^{-19}$ J at the superficial gas velocities of 0.35 and 0.6 m/s and presented in Fig. 4.
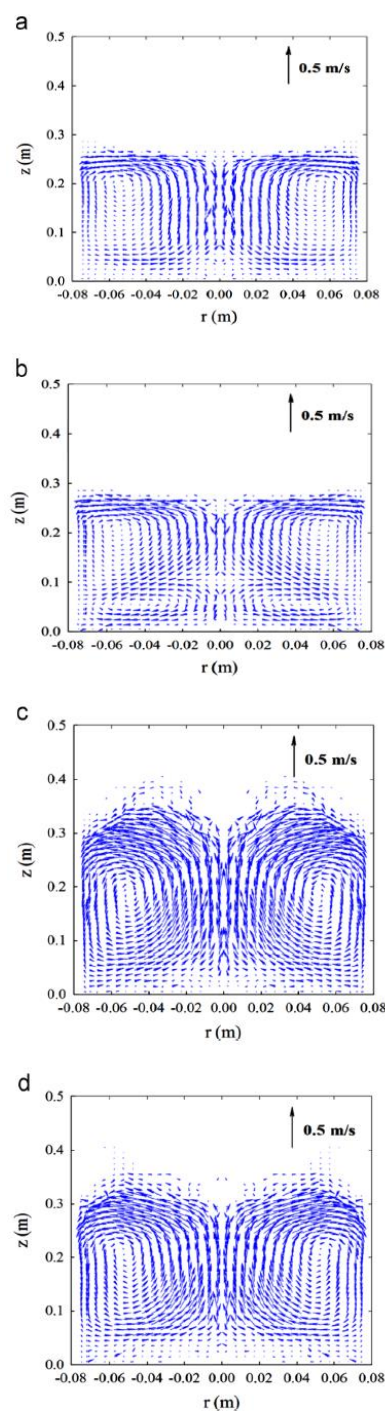
Figure 3. Effect of IPFs on the Eulerian velocity field of solids (a) SB20, U_g = 0.30 m/s, (b) CSB40, U_g = 0.30 m/s, (c) SB20, U_g = 0.50 m/s, (d) CSB40, U_g = 0.50 m/s [28].

According to Fig. 4, the solid flow pattern for bed with Hamaker constant of $7.2×10^{-19}$ at 0.35 m/s diverged from the typical pattern too. This deviation can be caused by a considerable amount of IPFs in the bed and low gas velocity, then it was

harder for the gas to break down the particle-particle contacts rather than the particle-wall contacts. Moreover, this figure depicts that increasing the superficial velocity results in increasing both the active height of the bed and the solid velocity. It can be further found from Fig. 4 that the particle average velocity decreases due to the presence of IPFs, which was reported by Willett [36] too. By comparing Fig. 3 with Fig. 4 It can be found that the scale of vertical and horizontal axes of these two figures are not the same. In our simulation results, these scales are the same and we see the side view of the bed as a rectangle in the simulation and as a square in the experiment. By considering this point and comparing Fig. 3 and Fig. 4, it can be concluded that the model used in this work can predict the solid flow pattern in experiments correctly. Therefore, at all velocities considered in this study (bubbling regime), the 2D Cartesian simulation can be acceptably predicted the results by the 3D cylindrical experiment.

4.2. Distribution of bed voidage

To determine the effect of IPF on the distribution of gas between emulsion and bubble phases, simulations were carried out with various values of Hamaker constant (i.e., various magnitudes of IPF). The probability density distribution of voidage at various Hamaker constants at the superficial gas velocities of 0.9 m/s are shown in Fig. 5. As mentioned before, such a distribution contains two peaks for emulsion phase and bubbles. It can be seen in this figure that by increasing the IPF, the peak of emulsion phase shifts to higher values. This means that the tendency of the fluidizing gas passing through the bed in the emulsion phase increases with increasing the IPF. In other words, by increasing the IPF in the bed, the emulsion phase can hold more gas between particles. Similar trends were reported by other researchers [26, 28, 39] concerning the effect of IPF on the emulsion voidage. This trend can be explained by the fact that existence of cohesive forces between particles leads to stickiness of particles which can hold a part of the particle weight. When particles collide, the particle-particle repulsion is less due the cohesive IPF which makes their movement to become limited. Therefore, particles cannot rearrange easily in the bed and particles cannot fill the cavities in their neighbors compared to the case when IPF is negligible. Consequently, increasing the IPF results in formation of more cavities between particles in emulsion phase which is observed as greater emulsion voidage.
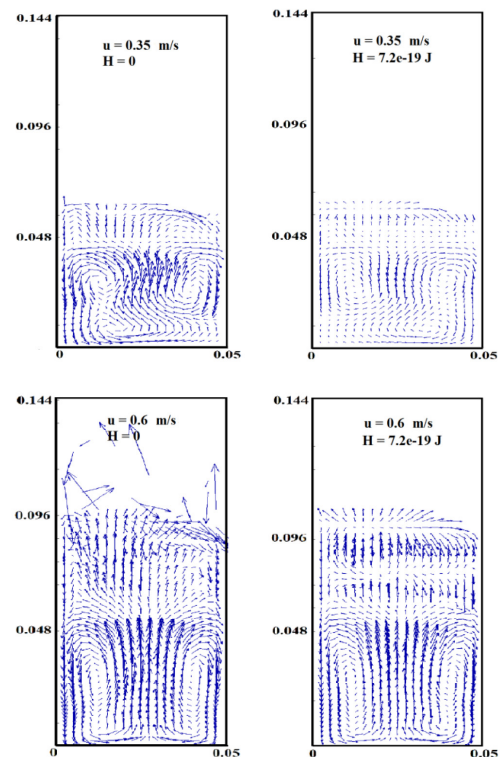
Figure 4. Effect of IPFs on the Eulerian velocity field of solids (a) H=0 J, U_g = 0.35 m/s, (b) H=3.6×10^{-19} J, U_g = 0.35 m/s, (c) H=0 J, U_g = 0.6 m/s, (d) H=3.6×10^{-19} J, U_g = 0.6 m/s

4.3. Bubble stability

The bubbles existence in bubbling fluidized beds can have dual effects on the bed behavior. For example, on one hand, existence of bubbles causes particles mixing in the fluidized beds, which results in an increase in mass and heat transfer rates in fluidized beds [35]. On another hand, contacts of the gaseous reactants in the bubble phase with the catalyst particles are difficult, hence, the presence of the bubbles results in decrease in the conversion of gaseous reactants in the fluidized bed reactor [26]. The effects of IPFs on the bubble stability in the bubbling fluidized beds were investigating with the help of computing the ratios of bubble coalescence to break up frequency. Frequencies of coalescence and break up of bubbles were calculated by counting the number of bubbles coalescence and bubbles splitting over a specified time interval. Observing more coales-

cences than break-ups reveals that bubbles are stable and increasing this difference is an indication of bubbles becoming more stable. The ratio of bubble coalescence to break up frequencies as a function of IPFs at the superficial gas velocity of 0.7 m/s is shown in Fig. 6. It shows that the ratio of frequencies increases with increasing the IPFs which indicates that bubbles are more stable in a fluidized bed with greater IPFs.
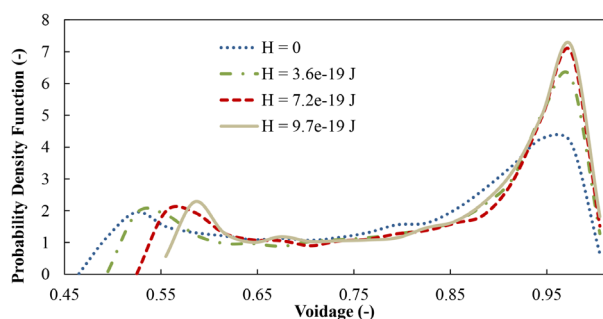
Figure 5. Probability density distribution of instantaneous local bed voidage at various values of IPFs at superficial gas velocities of 0.9 m/s

The frequency of bubble coalescence is greater than bubble break-up at various IPFs and bubbles grow in the bed with increasing the IPFs due to difference in coalescence and break-up rates. In fact, bubble breakage occurs due to instability in the bubble roof which lets a group of particles, in form of a finger, to fall through the void and leads to splitting of the bubble [5, 30]. When the IPFs is increased, particles mobility is reduced and emulsion phase resistance to structure change increases. Hence, formation of particle fingers falling from the roof of bubbles is reduced that leads to a decrease in bubble splitting and an increase in bubble stability.

4.4. Bubble diameter

In order to evaluate bubble diameter along the bed, the bed was divided into four sections. Fig. 7 shows these four sections which include one section near the distributor plate, A (corresponding to the height 2.4 cm), two middle sections, B and C (corresponding to heights 7.2 and 12 cm, respectively) and the last section near the top of the bed, D (corresponding to the height 16.8 cm). The equivalent diameter of bubbles was calculated by

recognizing boundaries of each bubble in fluid cells with $\varepsilon > 0.9$.
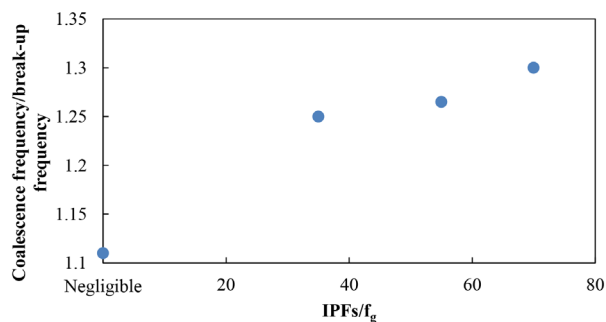
Figure 6. Ratio of the bubble coalescence and break up frequencies as a function of interparticle cohesive forces at superficial gas velocity of 0.7 m/s
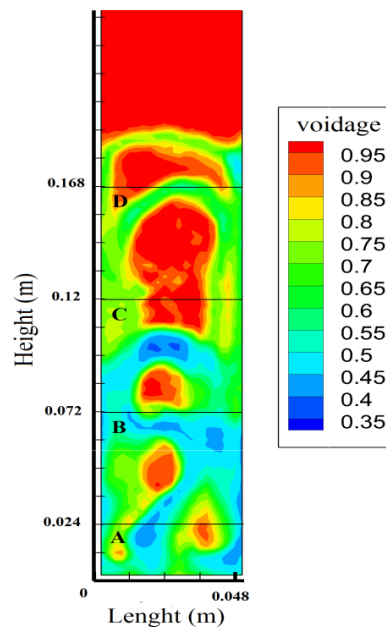
Figure 7. Four regions considered for calculating bubble diameter

Axial distribution of average bubble diameter in these four sections is plotted against the ratio of IPFs to weight of each particle in Fig. 8. It can be seen in this figure that bubbles are smaller near the distributor and they grow due to coalescence as they rise. Moreover, Fig. 8 demonstrates that introduction of the IPFs in the bed causes an increase in the bubble size. As mentioned before, addition of IPFs increases the tendency of particles to stick to each other and the bubble voidage increases, hence the boundary of the bubble ex-

pands and bubble size increases. With further increase in the IPFs the average bubble diameter slightly increases but not significantly.
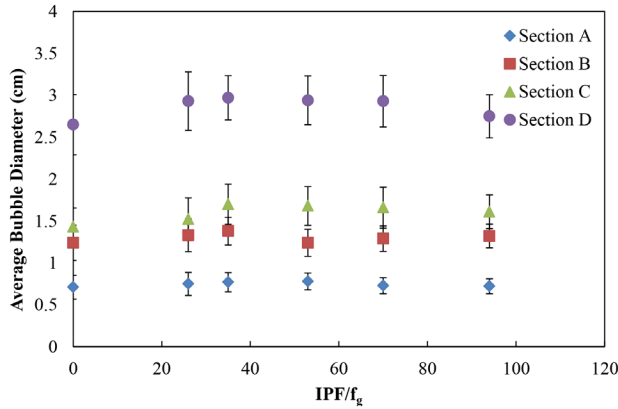
Figure 8. Effect of IPFs on the bubble diameter in four axial regions of the bed (error bars are 95% confidence interval)

4.5. Bubble rise velocity

Bubble rise velocity was determined from simulation in 2 sections A (corresponding to the height 9.6 cm) and B (corresponding to the height 14.4 cm), as shown in Fig. 9. The bubble rise velocity was obtained by tracking the center of individual bubbles in these sections in time. Velocity of the bubble center was then considered as the bubble rise velocity.

Fig. 10 illustrates the bubble rise velocity as a function of the level of IPFs in the above mentioned section at the superficial gas velocity of 0.9 m/s. This figure shows that the bubble rise velocity in both sections increases with increasing the level of IPFs. Physically, increasing the magnitude of adhesive IPFs leads to an increase in the dilution of emulsion phase which causes decrease in the density of emulsion phase. Besides, as mentioned before, the bubbles are larger in the presence of IPFs and bubble size slightly increases by enhancing the IPFs. In one hand, decrease in emulsion density causes decrease in drag and buoyancy forces. In another hand, increase in bubble diameter leads to increase in drag and buoyancy forces (increase in buoyancy force is greater than drag force due to stronger bubble diameter dependency of buoyancy force). Consequently, the buoyancy force become predominant against the drag force resistance on the bubble rising and the summation of acting forces on the bubble resulted in dragging the bubble upwards,

thus the bubble rise velocity increases. As it can be seen in the figure, the bubble rise velocity in section A is higher than in section B. Moreover, the difference between the bubble velocities in Sections A and B increases with elevating the IPFs. The bubbles rise and expand along the column and finally erupt at the bed surface. As we mentioned before, the bubble stability increases with the level of IPFs. This leads to the delayed eruption of bubbles at the bed surface and more decrease in the bubble rise velocity in section B.
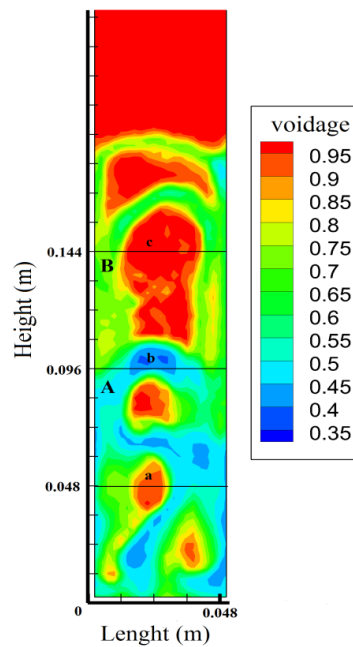
Figure. 9. Two regions for considered calculating the rise velocity of bubbles
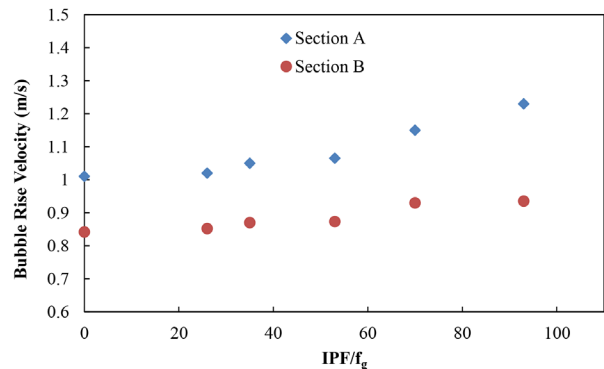
Figure 10. Effect of IPF on the bubble rise velocity along bed at superficial gas velocity of 0.9 m/s

5. Conclusions

A soft sphere CFD-DEM model was used to investigate the effect of IPF on the hydrodynamics of bubbling fluidized beds. The cohesive force between particles was considered to follow the van der Waals form. The code was validated by the experimental data in terms of probability density distribution of instantaneous local bed voidage and average velocity of particles. The simulation's results indicated that presence of IPFs in bed increases the tendency of the fluidizing gas passing through the bed in the emulsion phase. Increasing the level of IPFs in the bed increased the bubble stability and decreased the bubble break-up and hence bubbles became more stable. The results of bubble diameter showed that presence of IPFs forms larger bubbles in bed and increasing the level of IPFs leads to slightly increase in the bubble diameter. Also it was shown that increasing level of IPFs decreases the particle average velocity and increases bubble rise velocity. Existence of IPFs in the bed resulted in delayed bubble eruption at the bed surface which caused accumulation of bubbles at the top surface. Bubble eruption occurs harder by enhancing IPFs so the bubble rise velocity along the bed column decreased with higher IPFs.

Nomenclature

$\vec{f}_{d,i}$	drag force (N)
$\vec{f}^{c}_{ij}$	contact force (N)
$\vec{f}_{pf,i}$	fluid-particle interaction force (N)
$\vec{f}_{vdw,ik}$	van der Waals force between particles i and k (N)
$\vec{f}_{vdw}$	van der Waals force (N)
$\vec{f}_{vdw,i\rightarrow w}$	van der Waals force between particle i and wall (N)
$\vec{n}_{ij}$	unit vector
$\vec{r}$	position vector (m)
$\vec{u}$	fluid velocity (m.s^{-1})
$\vec{v}_i$	particle velocity (m.s^{-1})
$\vec{F}_{fp}$	average momentum exchange between fluid and solid (N)
$\vec{M}^{t}_{ij}$	torque in tangential direction (N.m)
$\vec{R}_i$	radius vector (from particle center to contact point) (m)
$\vec{V}_{r,ij}$	relative velocity of particles i and j (m.s^{-1})
C_d	drag coefficient
D_b	bubble diameter (m)
d_p	particle diameter (m)
f	frequency (Hz)
F_{co}	cohesive force (N)
f_g	gravitational force (N)
g	gravitational acceleration (m.s^{-2})
H	Hamaker constant (J)
H_{ap}	Hamaker constant of particles (J)
H_{aw}	Hamaker constant of particle and wall (J)
h_{ij}	displacement between surfaces of particle (m)
h_{iw}	displacement between particle i and wall (m)
I_i	moment of inertia (kg.m^2)
k_n	normal spring coefficient (N.m^{-1})
k_t	tangential spring coefficient (N.m^{-1})
L	bed height (m)
m_i	mass of particle i (kg)
N	number of positions
n_c	number of particles in contact with particle i
n_k	number of particles in Verlet list of particle i
P_F	fluid pressure (Pa)
R_i	axial position of bubble center (m)
RMS	root mean square (cm)
t	time (s)
U_g	superficial gas velocity (cm.s^{-1})
U_{mf}	minimum fluidization velocity (cm.s^{-1})
V_c	volume of computational cell (m^3)
$V_{p,i}$	volume of particle (m^3)

Greek symbols

α^{i}_{cell}	fractional area of particle i presenting in each cell
η_i	damping coefficient (m)
ω_i	angular velocity of particle i (s^{-1})
δ_n	deformation in the normal direction (m)
μ	inter-particle friction coefficient
μ_f	fluid viscosity (kg.m^{-1}.s^{-2})
δ_t	deformation in the tangential direction (m)
ε	local porosity
ε_b	bubble voidage
ε_e	emulsion phase voidage
ρ_f	fluid density (kg.m^{-3})
ρ_p	particle density (kg.m^{-3})
σ_r	mean square displacement (m^2)
τ	fluid viscose stress tensor (N.m^{-2})

References

[1] Agbim, J., Nienow, A., & Rowe, P. (1971). "Inter-particle forces that suppress bubbling in gas fluidised beds. "*Chemical Engineering Science,* Vol. 26, No. 8, pp. 1293-1294.

[2] Anderson, T. B., & Jackson, R. (1967). "Fluid mechanical description of fluidized beds. Equations of motion. "*Industrial & Engineering Chemistry Fundamentals,* Vol. 6, No. 4, pp. 527-539.

[3] Baerns, M. (1966). "Effect of interparticle adhesive forces on fluidization of fine particles. "*Industrial & Engineering Chemistry Fundamentals,* Vol. 5, No. 4, pp. 508-516.

[4] Bouffard, J., Bertrand, F., Chaouki, J., & Giasson, S. (2012). "Control of particle cohesion with a polymer coating and temperature adjustment. "*AIChE Journal,* Vol. 58, No. 12, pp. 3685-3696.

[5] Clift, R., Grace, J., & Weber, M. (1974). "Stability of bubbles in fluidized beds. "*Industrial & Engineering Chemistry Fundamentals,* Vol. 13, No. 1, pp. 45-51.

[6] Cundall, P.A., & Strack, O.D. (1979). "A discrete numerical model for granular assemblies. "*Geotechnique,* Vol. 29, No. 1, pp. 47-65.

[7] Dahneke, B. (1972). "The influence of flattening on the adhesion of particles. "*Journal of Colloid and Interface Science,* Vol. 40, No. 1, pp. 1-13.

[8] Di Felice, R. (1994). "The voidage function for fluid-particle interaction systems. "*International Journal of Multiphase Flow,* Vol. 20, No. 1, pp. 153-159.

[9] Feng, Y., & Yu, A. (2004). "Assessment of model formulations in the discrete particle simulation of gas-solid flow. "*Industrial & Engineering Chemistry Research,* Vol. 43, No. 26, pp. 8378-8390.

[10] Geldart, D. (1973). "Types of gas fluidization. "*Powder Technology,* Vol. 7, No. 5, pp. 285-292.

[11] Geldart, D., & Abrahamsen, A. R. (1978). "Homogeneous fluidization of fine powders using various gases and pressures. "*Powder Technology,* Vol. 19, No. 1, pp. 133-136.

[12] Geldart, D., Harnby, N., & Wong, A. (1984). "Fluidization of cohesive powders. "*Powder Technology,* Vol. 37, No. 1, pp. 25-37.

[13] Hassani, M. A., Zarghami, R., Norouzi, H., & Mostoufi, N. (2013). "Numerical investigation of effect of electrostatic forces on the hydrodynamics of gas–solid fluidized beds. "*Powder Technology,* Vol. 246, pp. 16-25.

[14] Kobayashi, T., Tanaka, T., Kawaguchi, T., Mukai, T., & Tsuji, Y. (2006). "DEM analysis on flow patterns of Geldart's group A particles in fluidized bed. "*Journal of the Society of Powder Technology, Japan,* Vol. 43, No. 10, pp. 737-745.

[15] Kobayashi, T., Kawaguchi, T., Tanaka, T., & Tsuji, Y. (2003). "DEM analysis of fluidized behaviour of Geldart's Group A particles (pressure drop and stress distribution). "*Paper presented at the Proceeding of The second Asian Particle Technology Symposium*, pp. 17-19.

[16] Kobayashi, T., Tanaka, T., Shimada, N., & Kawaguchi, T. (2013). "DEM–CFD analysis of fluidization behavior of Geldart Group A particles using a dynamic adhesion force model. "*Powder Technology,* Vol. 248, pp. 143-152.

[17] Kruggel-Emden, H., Wirtz, S., & Scherer, V. (2008). "A study on tangential force laws applicable to the discrete element method (DEM) for materials with viscoelastic or plastic behavior. "*Chemical Engineering Science,* Vol. 63, No. 6, pp. 1523-1541.

[18] Lettieri, P., Newton, D., & Yates, J. (2001). "High temperature effects on the dense phase properties of gas fluidized beds. "*Powder Technology,* Vol. 120, No. 1, pp. 34-40.

[19] Lettieri, P., Yates, J., & Newton, D. (2000). "The influence of interparticle forces on the fluidization behaviour of some industrial materials at high temperature. "*Powder Technology,* Vol. 110, No. 1, pp. 117-127.

[20] McLaughlin, L. J., & Rhodes, M. J. (2001). "Prediction of fluidized bed behaviour in the presence of liquid bridges. "*Powder Technology,* Vol. 114, No. 1, pp. 213-223.

[21] Morooka, S., Kusakabe, K., Kobata, A., & Kato, Y. (1988). "Fluidization state of ultrafine powders. "*Journal of Chemical Engineering of Japan,* Vol. 21, No. 1, pp. 41-46.

[22] Norouzi, H. R., Mostoufi, N., Zarghami, R., & Sotudeh-Gharebagh, R. (2016). *Coupled CFD-DEM Modeling: Formulation, Implementation and Application to Multiphase Flows*: John Wiley & Sons.

[23] Pandit, J. K., Wang, X., & Rhodes, M. (2007). "A DEM study of bubble formation in Group B fluidized beds with and without cohesive inter-particle forces. "*Chemical Engineering Science,* Vol. 62, No. 1, pp. 159-166.

[24] Patankar, S. (1980). Numerical heat transfer and fluid flow: *CRC press.*

[25] Rhodes, M., Wang, X., Nguyen, M., Stewart, P., & Liffman, K. (2001). "Use of discrete element method simulation in studying fluidization characteristics: influence of interparticle force. "*Chemical Engineering Science,* Vol. 56, No. 1, pp. 69-76.

[26] Rowe, P., Santoro, L., & Yates, J. (1978). "The division of gas between bubble and interstitial phases in fluidised beds of fine powders." *Chemical Engineering Science,* Vol. 33, No. 1, pp. 133-140.

[27] Seville, J., & Clift, R. (1984). "The effect of thin liquid layers on fluidisation characteristics. "*Powder Technology,* Vol. 37, No. 1, pp. 117-129.

[28] Shabanian, J., & Chaouki, J. (2014). "Local characterization of a gas–solid fluidized bed in the presence of thermally induced interparticle forces. "*Chemical Engineering Science,* Vol. 119, pp. 261-273.

[29] Shabanian, J., & Chaouki, J. (2015). "Hydrodynamics of a gas–solid fluidized bed with thermally induced interparticle forces. "*Chemical Engineering Journal,* Vol. 259, pp. 135-152.

[30] Shabanian, J., & Chaouki, J. (2017). "Similarities between gas-solid fluidization in the presence of interparticle forces at high temperature and induced by a polymer coating approach. "*Powder Technology*, Vol.320, pp.155-160.

[31] Shabanian, J., Fotovat, F., Chaouki, J., & Bouffard, J. (2011). "Fluidization behavior in a gas-solid fluidized bed with thermally induced inter-particle forces. "10th International Conference on Circulating Fluidized Beds and Fluidization Technology - CFB-10, T. Knowlton, PSRI Eds, ECI Symposium Series.

[32] Si, C., & Guo, Q. (2008). "Wavelet analysis of particle concentration signals in an acoustic bubbling fluidized bed. "*Chemical engineering & technology,* Vol. 31, No. 1, pp. 1597-1604.

[33] Tatemoto, Y., Mawatari, Y., & Noda, K. (2005). "Numerical simulation of cohesive particle motion in vibrated fluidized bed. "*Chemical Engineering Science,* Vol. 60, No. 18, pp. 5010-502*1*.

[34] Tsuji, Y., Kawaguchi, T., & Tanaka, T. (1993). "Discrete particle simulation of two-dimensional fluidized bed. "*Powder Technology,* Vol. 77, No. 1, pp. 79-87.

[35] Van der Schaaf, J., Schouten, J., Johnsson, F., & Van den Bleek, C. (2002). "Non-intrusive determination of bubble and slug length scales in fluidized beds by decomposition of the power spectral density of pressure time series. "*International Journal of Multiphase Flow,* Vol. 28, No. 5, pp. 865-880.

[36] Willett, C. (1999). *The Micromechanics of Wet Particulate Materials.* PhD Thesis, University of Birmingham.

[37] Xu, B., & Yu, A. (1997). "Numerical simulation of the gas-solid flow in a fluidized bed by combining discrete particle method with computational fluid dynamics. "*Chemical Engineering Science,* Vol. 52, No. 16, pp. 2785-2809.

[38] Yao, W., Guangsheng, G., Fei, W., & Jun, W. (2002). "Fluidization and agglomerate structure of SiO 2 nanoparticles. "*Powder Technology,*Vol. 124, No. 1, pp. 152-159.

[39] Yates, J., & Newton, D. (1986). "Fine particle effects in a fluidized-bed reactor. "*Chemical Engineering Science,* Vol. 41, No. 4, pp. 801-806.

[40] Ye, M., Van der Hoef, M., & Kuipers, J. (2004). "A numerical study of fluidization behavior of Geldart A particles using a discrete particle model. "*Powder Technology,* Vol. 139, No. 2, pp. 129-139.

[41] Yu, A. B., & Xu, B. H. (2003). "Particle-scale modelling of gas–solid flow in fluidisation. "*Journal of Chemical Technology and Biotechnology,* Vol. 78, No. 2-3, pp. 111-121.